Journal of Materials Chemistry A

PAPER

View Article Online
View Journal | View Issue

Cite this: J. Mater. Chem. A, 2019, 7, 25314

Highly flexible and sensitive temperature sensors based on $Ti_3C_2T_x$ (MXene) for electronic skin†

Zherui Cao,‡[ab] Yina Yang,‡[ab] Yinghui Zheng,[c] Wei Wu,[d] Fangfang Xu,[a] Ranran Wang*[a] and Jing Sun [a]

Received 22nd August 2019
Accepted 9th October 2019

DOI: 10.1039/c9ta09225k

rsc.li/materials-a

Electronic skin (e-skin) has been attracting great research interest and effort due to its potential applications in wearable health monitoring devices, smart prosthetics, humanoid robots and so on. Temperature is an important parameter for e-skin to perceive surroundings and people. However, little research has been carried out in the field of flexible temperature sensing and current temperature sensors still face many challenges in practical applications, such as high sensing performance, facile preparation, and differentiating from other stimuli. Herein, we develop a facile fabrication strategy for $Ti_3C_2T_x$ based temperature sensors. As the sensing units, $Ti_3C_2T_x$ nanoparticles and lamellae can be obtained simultaneously through controlling the fabrication conditions. These temperature sensors exhibit tunable sensing performances and a desirable combination of a high sensitivity (up to 986 $°C^{-1}$) and a wide working range (140 °C). Due to their high sensitivity, these sensors can also be used as e-skin for proximity detection and illumination detection from ultraviolet to infrared light. For application demonstration, a 4 × 4 array of the sensors was fabricated for temperature mapping, indicating their great potential for monitoring approaching objects and temperature variations.

Introduction

As one of the most important subfields of flexible electronics, electronic skin (e-skin) has been an active area of research for decades.[1–7] Skin is the largest organ of the body, in which there are sorts of receptors that differentiate and measure multiple environmental stimuli.[8–11] E-skin containing sensors with various functionalities can mimic the sensing properties of human skin, which indicates its promising utilization in smart medical diagnostics[12,13] and humanoid robots.[14,15] So far, most studies have focused on the development of pressure sensors for e-skin. The properties of pressure sensors such as sensitivity and response range have been significantly improved, owing to the progress of novel materials[16–23] and structural engineering.[24–28] The developments in fabrication techniques can satisfy most of the requirements for the mechanical sensing properties of e-skin. By contrast, their ability to respond to other environmental stimuli (*e.g.*, temperature, humidity and gas) has been ignored.[29–34] As an important parameter, temperature plays an irreplaceable role in the sensing of surroundings and people. Further studies of temperature sensors can contribute to the development of multifunctional and integrated sensing systems, significantly broadening the application scope of e-skin.

The sensing performances of most temperature sensors are based on changes in electrical characteristics of temperature-sensitive materials. Traditional temperature sensors made of bulky and rigid materials are inappropriate for e-skin because of their poor mechanical compliance.[35–38] Recently, some temperature sensors were fabricated by incorporating novel materials including organic semiconductors,[39,40] carbon nanotubes (CNTs),[41,42] and graphene[43,44] into elastomer substrates to extend their capabilities such as flexibility and stretchability. Nonetheless, existing flexible temperature sensors still suffer from many limitations, which impede their further development. For example, relatively low sensitivity and accuracy restrict rapid and precise temperature monitoring, which cannot satisfy the demands for e-skin under all conditions.[45–47]

[a]State Key Laboratory of High Performance Ceramics and Superfine Microstructure, Shanghai Institute of Ceramics, Chinese Academy of Sciences, 1295 Ding Xi Road, Shanghai 200050, P. R. China. E-mail: wangranran@mail.sic.ac.cn

[b]University of Chinese Academy of Sciences, 19 Yuquan Road, Beijing 100049, P. R. China

[c]State Key Laboratory of High Field Laser Physics, Shanghai Institute of Optics and Fine Mechanics, Chinese Academy of Sciences, Shanghai 201800, China

[d]Thermo Fisher Scientific, China

† Electronic supplementary information (ESI) available: TEM images of $Ti_3C_2T_x$, AFM results of $Ti_3C_2T_x$, response time curves of the $Ti_3C_2T_x$ based sensors, resistance variation *versus* temperature of the $Ti_3C_2T_x$ based sensors during the first cycle, length variation *versus* temperature of a PDMS block, resistance variation *versus* strain of the $Ti_3C_2T_x$ based sensors, microstructure variations of the cracks of the TMA-$Ti_3C_2T_x$ film during the heating process, resistance variation *versus* pressure of the $Ti_3C_2T_x$ based sensors, the test method for the temperature sensing performance, resistance variation *versus* temperature of the $Ti_3C_2T_x$ based sensors measured using an infrared imaging device, comparison of the typical sensing properties reported in the previous studies. See DOI: 10.1039/c9ta09225k

‡ These authors contributed equally to this work.

Additionally, current methods used for the fabrication of temperature sensors require large-scale integration of high-performance electronic components (*e.g.*, field-effect transistors) on flexible substrates.[48–50] These and other related technologies involve special processing steps and complex fabrication designs, which also influence the comfort of devices in practical applications. Moreover, most temperature sensors need to come in contact with measuring objects to detect temperatures.[51–53] For temperature sensors with high sensitivity, external forces may interfere with the detection of temperature. It is still difficult to differentiate the temperature signal from the response to other stimuli.

Herein, we fabricated a flexible temperature sensor facilely by incorporating novel $Ti_3C_2T_x$ nanoparticle–lamella hybrid networks into polydimethylsiloxane (PDMS) substrates. The sensor exhibited a high sensitivity (up to 986 $°C^{-1}$) and a wide response range (140 °C) due to the specific hybrid conductive network of $Ti_3C_2T_x$ and a large coefficient of thermal expansion of PDMS. Furthermore, the sensor possessed a fast response time (6.3 s), a high accuracy (0.1 °C), and good reliability and durability (>100 cycles), which could satisfy the requirements of e-skin for temperature monitoring. To the best of our knowledge, both the sensitivity and response range of our flexible temperature sensor surpass the performances of its previously reported counterparts. To disclose the underlying mechanism, the morphological evolution of $Ti_3C_2T_x$ was characterized by scanning electron microscopy (SEM) under *in situ* heating. In addition to temperature monitoring in the contact mode, the sensor was also applied for proximity detection where the largest distance of detecting an approaching finger is 9 cm. Moreover, the temperature sensor can detect illumination from ultraviolet to infrared light, which extends the application scope of the sensor for noncontact detection. Finally, a 4 × 4 array of the temperature sensors was fabricated for full operational demonstration of e-skin. The corresponding mapping of the temperature distribution was obtained *via* the measurements of the resistance variations by stimulating the pixels with various heat sources, confirming their great potential in wearable skin electronics for monitoring both approaching objects and temperature variations during daily activities.

Results and discussion

Fig. 1a illustrates the schematic of the fabrication process of the $Ti_3C_2T_x$/PDMS composite film. $Ti_3C_2T_x$ was produced mainly by two steps, etching and delamination. Initially, Al layers in

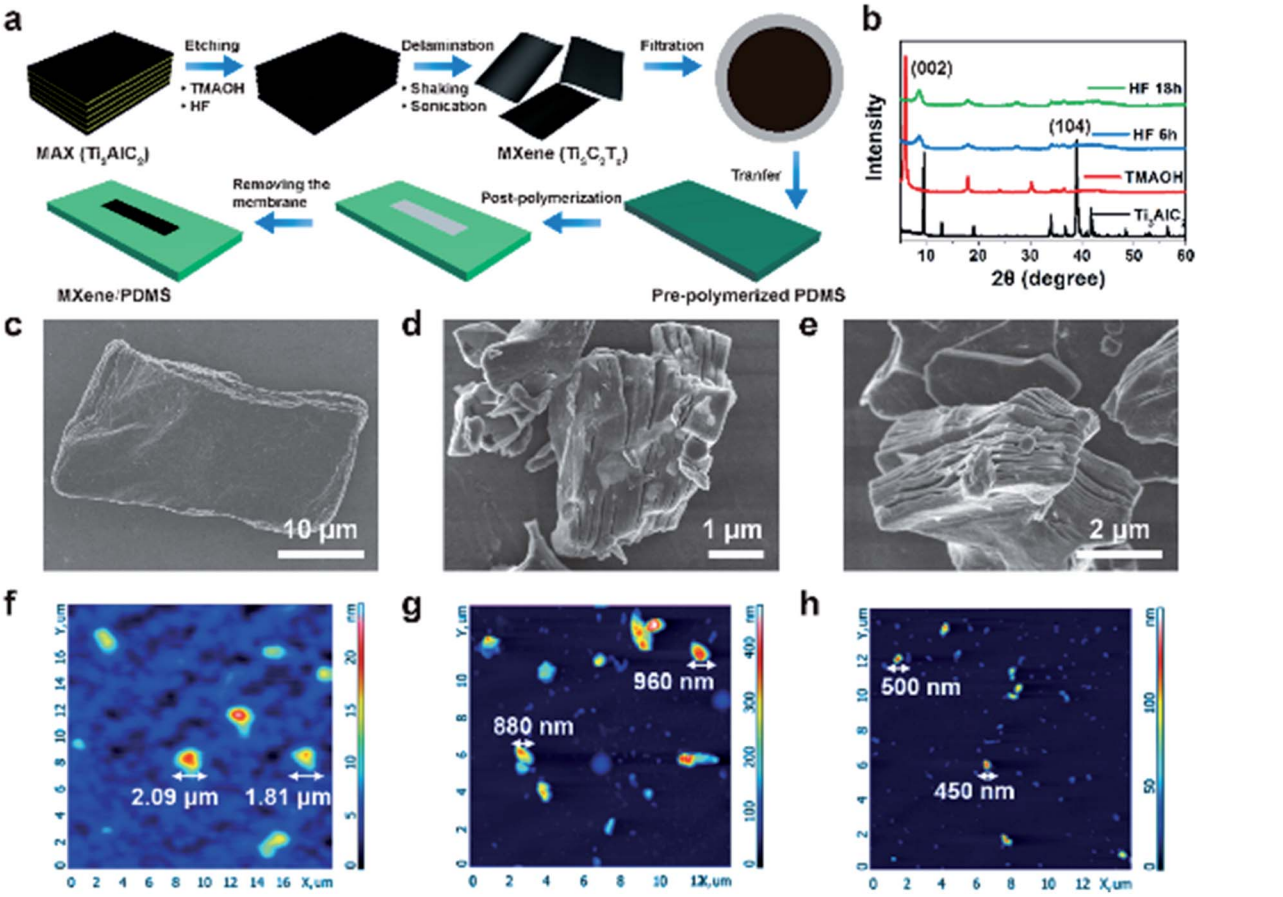

Fig. 1 (a) The schematic illustration of the fabrication of the $Ti_3C_2T_x$/PDMS film. (b) XRD patterns of the pristine Ti_3AlC_2 and multilayer $Ti_3C_2T_x$ obtained under three processing conditions. SEM images of the multilayer $Ti_3C_2T_x$ treated with TMAOH for 24 h (c), HF for 6 h (d), and HF for 18 h (e). AFM images of TMA-$Ti_3C_2T_x$ (f), HF6-d3-$Ti_3C_2T_x$ (g), and HF18-d2-$Ti_3C_2T_x$ (h).

Ti_3AlC_2 phases were selectively etched with TMAOH or HF aqueous solution with different concentrations for different time duration. Subsequently, mono- or few-layer $Ti_3C_2T_x$ flakes were obtained through delamination (handshaking or sonication). The $Ti_3C_2T_x$ film was prepared by vacuum filtering the $Ti_3C_2T_x$ suspension using a mixed cellulose ester (MCE) membrane. Then the $Ti_3C_2T_x$/MCE filter membrane was transferred to the pre-polymerized PDMS substrates and they were fully post-polymerized. Finally, the $Ti_3C_2T_x$/PDMS composite film was prepared after dissolving the filter membrane in acetone.

The flake size and quality of $Ti_3C_2T_x$ can be controlled by adjusting the etching and delamination conditions including etchants, etching duration, delamination methods and duration. The final $Ti_3C_2T_x$ samples are referred to as "TMA-$Ti_3C_2T_x$" and "HF*y*-d*z*-$Ti_3C_2T_x$" corresponding to the process conditions, in which TMA and HF represent the treatment with TMAOH or HF, where *y* stands for the hours of etching and *z* stands for the hours of sonication. The structure of the pristine Ti_3AlC_2 and multilayer $Ti_3C_2T_x$ obtained under three conditions was characterized by X-ray diffraction (XRD; Fig. 1b). The diffraction peak of the (104) planes of Ti_3AlC_2 was absent in the XRD patterns of multilayer $Ti_3C_2T_x$, suggesting the successful removal of the Al layers by etching. In addition, the diffraction peak of the (002) plane was observed to shift toward lower angles, indicating a broader interspace of the former. The variety among the peaks was attributed to the different etching intensity of TMAOH and HF. After etching with TMAOH or HF, the flakes showed a thick paper morphology (Fig. 1c) and an accordion-like structure (Fig. 1d and e), respectively. Fig. 1f–h and S1a–c† show the atomic force microscopy (AFM) and transmission electron microscopy (TEM) images of the structure of the $Ti_3C_2T_x$ flakes obtained after delamination, respectively. The multilayer $Ti_3C_2T_x$ was exfoliated into monolayer nanosheets with different lateral dimensions. Because the interlayer spacing of the $Ti_3C_2T_x$ etched with TMAOH was larger than that of the $Ti_3C_2T_x$ etched with HF, thinner lamellae were prepared through delamination.

To further explore the effect of different processing conditions on the morphologies of $Ti_3C_2T_x$ flakes, the 3D morphology size statistics of the three kinds of $Ti_3C_2T_x$ were investigated by AFM as shown in Fig. S2a–i.† The TMA-$Ti_3C_2T_x$ sample was mainly composed of thin and large monolayers, which exhibited a thickness of 15–20 nm and a lateral size of about 2 μm (Fig. S2a–c†), while $Ti_3C_2T_x$ etched with HF was considered as a mixture of random nanoparticles and 2D stacked lamellae with diverse thicknesses. The HF18-d2-$Ti_3C_2T_x$ sample was composed of lamellae with a lateral size of about 500 nm and some nanoparticles with a similar thickness and lateral sizes of 100 to 120 nm (Fig. S2g–i†). As for HF6-d3-$Ti_3C_2T_x$, the lateral size of the lamellae and the thickness of the random nanoparticles were 900 and 320–380 nm, respectively, which were much larger than those of HF18-d2-$Ti_3C_2T_x$ due to the shorter etching time duration (Fig. S2d–f†).

The $Ti_3C_2T_x$ film was prepared by vacuum filtering the $Ti_3C_2T_x$ suspension using a MCE membrane. Fig. 2a–f show the top view and cross-sectional SEM images of $Ti_3C_2T_x$/MCE membranes obtained under different processing conditions. As shown in Fig. 2a, the TMA-$Ti_3C_2T_x$ sample was a paper-like dense and uniform membrane with more flat surfaces than those of HF6-d3-$Ti_3C_2T_x$ (Fig. 2b) and HF18-d2-$Ti_3C_2T_x$ (Fig. 2c). By contrast, the films of HF6-d3-$Ti_3C_2T_x$ and HF18-d2-$Ti_3C_2T_x$ displayed a multi-dimensional hybrid network consisting of random nanoparticles and lamellae. The nanoparticles stacked randomly to form a loose and porous microstructure and lamellae served as bridges to realize connections in the conductive network. The cross-sectional SEM images of the TMA-$Ti_3C_2T_x$, HF6-d3-$Ti_3C_2T_x$, and HF18-d2-$Ti_3C_2T_x$ films on the MCE membrane are shown in Fig. 2d–f. The thickness of the films obtained using TMAOH and HF was about 400 and 900 nm, respectively. The HF-$Ti_3C_2T_x$ film was more loose and rougher than the TMA-$Ti_3C_2T_x$ film because of its nanoparticles with diverse sizes and irregular shapes. Therefore, the resistance of the HF-$Ti_3C_2T_x$ film was larger than that of the TMA-$Ti_3C_2T_x$ film. The $Ti_3C_2T_x$ films also presented diverse morphologies after being transferred to PDMS (Fig. 2g–i). From the top-view SEM images of Fig. 2g, some cracks on the surface of the TMA-$Ti_3C_2T_x$ film were observed because PDMS swelled when immersed in acetone, which led to the expansion of the $Ti_3C_2T_x$ network. Due to the considerable mismatch of the moduli between the conductive layer and the elastic substrate, the displacements of the compact lamellae developed into cracks in the stress concentration area, which could not recover completely. In contrast, the HF6-d3-$Ti_3C_2T_x$ film with random nanoparticles deformed with the substrate to release the stress, which only caused fine cracks. Because of the shrinkage of the substrate after drying, the film developed buckles due to the lateral pressure. The surface of HF18-d2-$Ti_3C_2T_x$ exhibited crumples without obvious cracks, which can be attributed to better stretchability of the film.

We chose PDMS as the flexible substrate because of its large coefficient of thermal expansion. When the temperature of the sensors increased, the expansion of PDMS led to the stretching of the conductive network, which resulted in the resistance variation. The current–voltage (*I*–*V*) curves of the HF6-d3-$Ti_3C_2T_x$-$Ti_3C_2T_x$ based sensors with a pre-polymerization time of 10 min as a function of temperature show that the current decreased when the temperature was varied from 25 to 65 °C (Fig. 3a). The sensors exhibited an ohmic behavior irrespective of temperature and the resistance monotonically increased with the temperature. The pre-polymerization duration is another important factor that influences the sensing properties. Fig. 3b exhibits the resistance variation *versus* temperature of the TMA-$Ti_3C_2T_x$ based sensors with different pre-polymerization times from 5 min to 15 min. R/R_0 increased faster for the sensors with a longer pre-polymerization time while the sensing range of the sensors extended as the pre-polymerization time decreased. It can be explained by the fact that a shorter pre-polymerization time leads to a deeper embedment of $Ti_3C_2T_x$ into PDMS, which enhanced the binding force between the conductive network and the substrate. The response of the sensors to continuous temperature variations was investigated by measuring the resistance changes over the temperature range from 25 to 140 °C (Fig. 3c). The base-10 logarithm of the resistance change

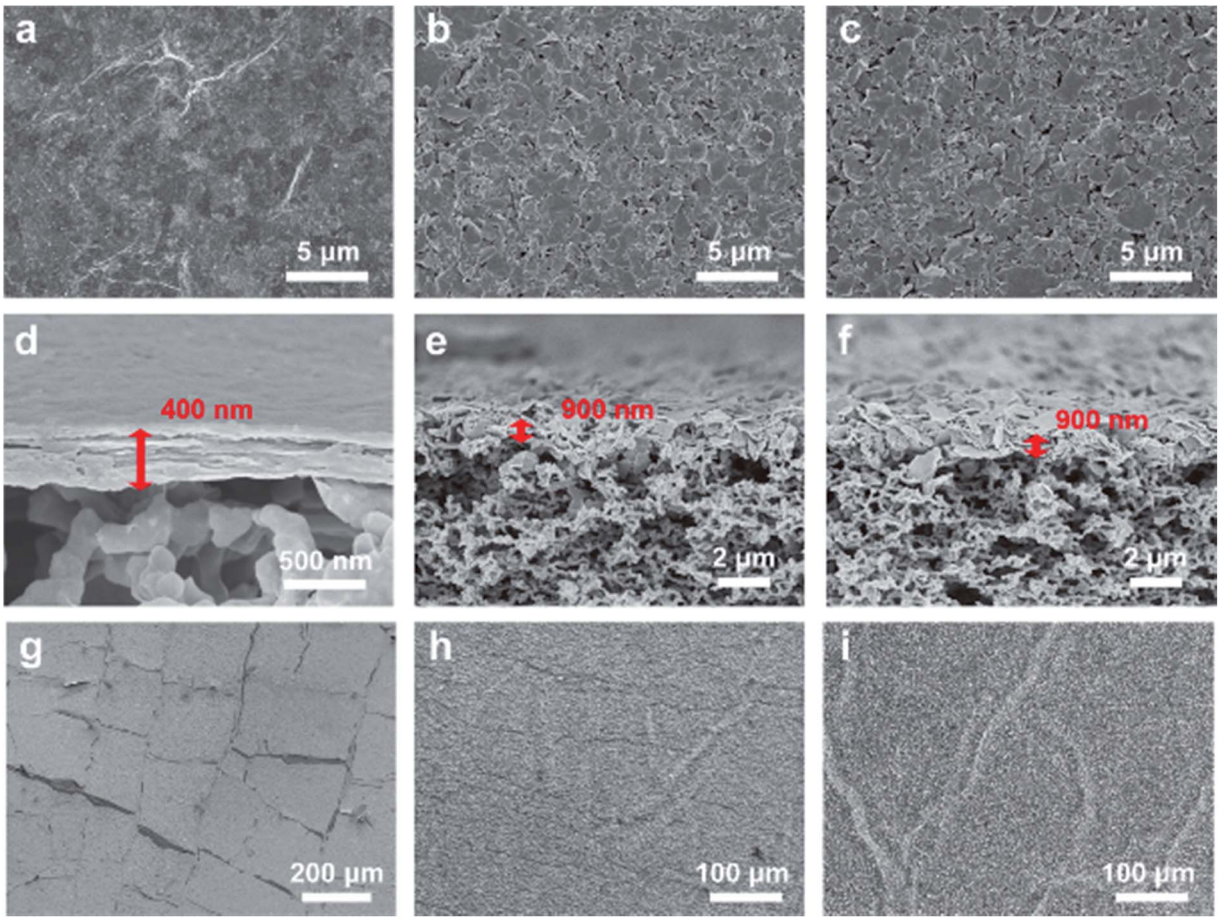

Fig. 2 (a–c) Top-view SEM images of the TMA-$Ti_3C_2T_x$ (a), HF6-d3-$Ti_3C_2T_x$ (b), and HF18-d2-$Ti_3C_2T_x$ (c) films on the MCE membrane. (d–f) Cross-sectional SEM images of the TMA-$Ti_3C_2T_x$ (d), HF6-d3-$Ti_3C_2T_x$ (e), and HF18-d2-$Ti_3C_2T_x$ (f) films on the MCE membrane. (g–i) Top view SEM images of the TMA-$Ti_3C_2T_x$ (g), HF6-d3-$Ti_3C_2T_x$ (h), and HF18-d2-$Ti_3C_2T_x$ (i) films on the PDMS substrates.

exhibited almost linear dependence on the temperature and the plot showed that the three kinds of $Ti_3C_2T_x$ based sensors with the pre-polymerization time of 10 min exhibited different temperature responses. For the TMA-$Ti_3C_2T_x$ based sensors, the resistance dramatically increased over the temperature range from 25 to 60 °C, representing about a 10^4 fold variation. In contrast, the HF18-d2-$Ti_3C_2T_x$ based sensors showed about an 800 fold variation over the large temperature range from 25 to 140 °C. The performance of the HF6-d3-$Ti_3C_2T_x$ based sensors was intermediate between those of the above two samples, which exhibited both a large resistance variation and a wide working range. This excellent performance can satisfy the demands of temperature sensors on most occasions. The slope of the curve is related to the sensitivity, which is a key characteristic parameter of the temperature sensor and is defined as $(R - R_0/R_0)/\Delta T$, where ΔT is the temperature change. The sensitivities of the TMA-$Ti_3C_2T_x$, HF6-d3-$Ti_3C_2T_x$ and HF18-d2-$Ti_3C_2T_x$ based sensors were quantified as 1.71 to 987, 0.03 to 503 and 0.07 to 17, respectively. As shown in Fig. 3d and Table S1,† the sensitivity and sensing ranges were much larger than those of the previously reported temperature sensors.[41,43,45–47,54–59] To balance the sensitivity and the working range, we chose the HF6-d3-$Ti_3C_2T_x$ based sensors with the pre-polymerization time of 10 min for the measurement and demonstration of other sensing properties. To measure the response time of the sensors, we raised the temperature of the sensors and measured the resistance and temperature changes, respectively. The time difference was as short as 6.3 s as shown in Fig. S3.† The accuracy of the sensors was determined to be 0.1 °C (Fig. 3e). The high accuracy was appropriate for the rapid and precise temperature monitoring under various conditions. Furthermore, the durability-test results of 100 heating cycles (25 to 50 °C) are plotted in Fig. 3f. The overall trend of the resistance variations remained the same, especially for the curves overlapped in the range from 25 to 40 °C while they did not coincide perfectly from 45 to 50 °C. The resistance variation of the sensors at 50 °C after 100 cycles rose about 50% compared with that in the first test due to the incomplete recovery of the microstructure of the $Ti_3C_2T_x$ film after the expansion–shrinkage process. Some fractures or even exfoliation could occur in the conductive network. To reduce the signal change during long-term cycling, the sensors could be encapsulated with PDMS to reinforce the adhesion between the sensitive material and substrate, which enhanced their stability. Even so,

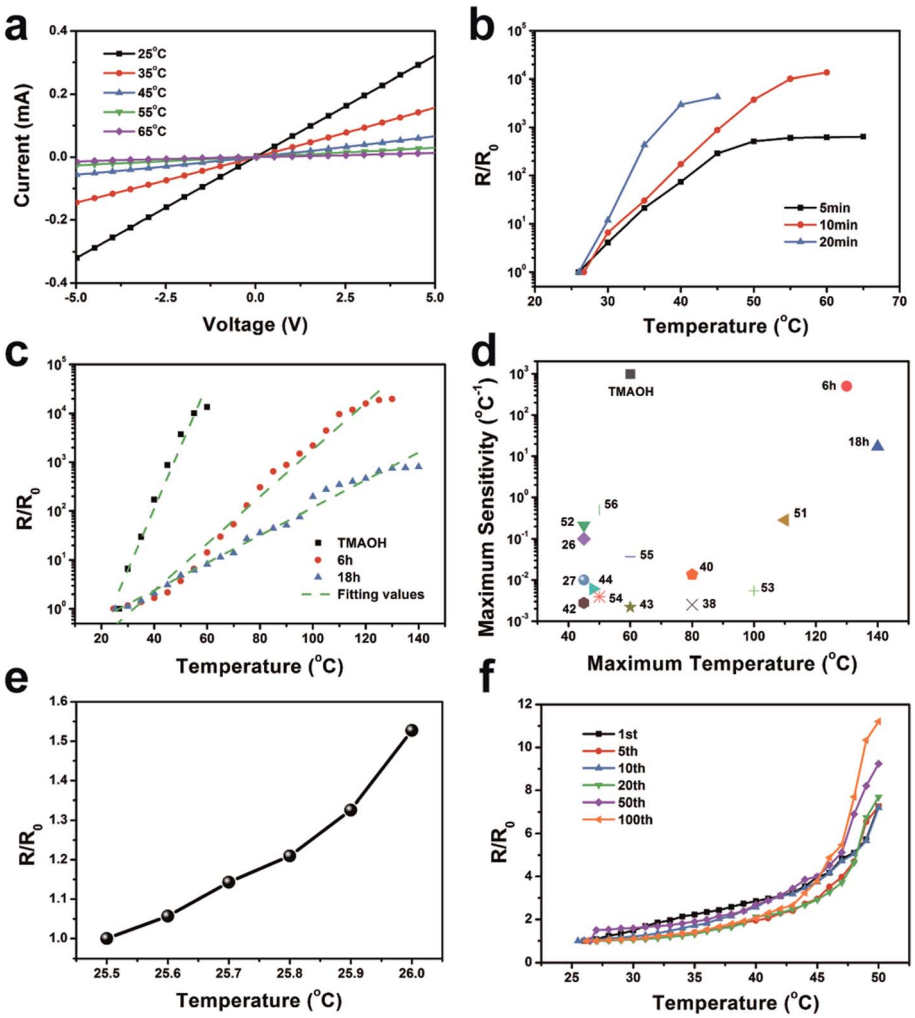

Fig. 3 (a) Current–voltage curves of the $Ti_3C_2T_x$ based sensors at different temperatures. (b) Resistance variations *versus* temperatures of the $Ti_3C_2T_x$ based sensors with different pre-polymerization times from 5 min to 15 min. (c) Resistance variations *versus* temperatures of the three kinds of $Ti_3C_2T_x$ based sensors. (d) Summary of the reported values of the maximum sensitivity and the maximum sensing temperature from the literature and results from this work. (e) Resistance variations of the $Ti_3C_2T_x$ based sensors under subtle temperature changes. (f) Resistance variations of the $Ti_3C_2T_x$ based sensors during cycling tests: 1st (black), 5th (red), 10th (blue), 20th (green), 50th (purple), and 100th (orange) cycles at temperatures from 25 to 50 °C.

the cycling performance was remarkable among the reported temperature sensors fabricated with the novel sensitive materials. Fig. S4† shows the resistance variation of the sensors in the temperature range from 26 to 43 °C during the first cycle. The resistance variation increased linearly with the increase of temperature ($R/R_0 = 0.13306T - 2.46724$, the degree of fitting is 0.9971). The high linearity and repeatability confirmed the reliability for practical applications such as daily wearable temperature sensors.

To disclose the underlying response mechanism of the $Ti_3C_2T_x$-PDMS temperature sensors, we employed SEM to observe the morphological evolution of the $Ti_3C_2T_x$ network upon varying the temperature from 25 to 150 °C. Fig. 4 exhibits the top-view SEM images of the TMA-$Ti_3C_2T_x$, HF6-d3-$Ti_3C_2T_x$, and HF18-d2-$Ti_3C_2T_x$ based sensors with the pre-polymerization time of 10 min under *in situ* heating. The TMA-$Ti_3C_2T_x$ film was mainly composed of tightly stacked large-size lamellae with tiny cracks formed during the fabrication process before being heated. As shown in Fig. 4a–d, the TMA-$Ti_3C_2T_x$ film was subjected to an omnidirectional tensile stress with the uniform expansion of PDMS when the temperature was raised from 25 to 150 °C. To further demonstrate the effect of the omnidirectional expansion on the sensing performance of the temperature sensors, we compared the resistance variations under unidirectional stretching with those under heating. Fig. S5† presents the length variation *versus* temperature of a PDMS block (25 × 5 × 5 mm). The length of PDMS increased 3.79% with the increase of temperature from 25 to 100 °C. The resistance variations of the three kinds of temperature sensors with the pre-polymerization time of 10 min under unidirectional stretching are plotted in Fig. S6.† The resistance variation at a tensile strain of 4% was much less than that at the corresponding temperature (Fig. 3b), revealing the larger change of the conductive network under uniform

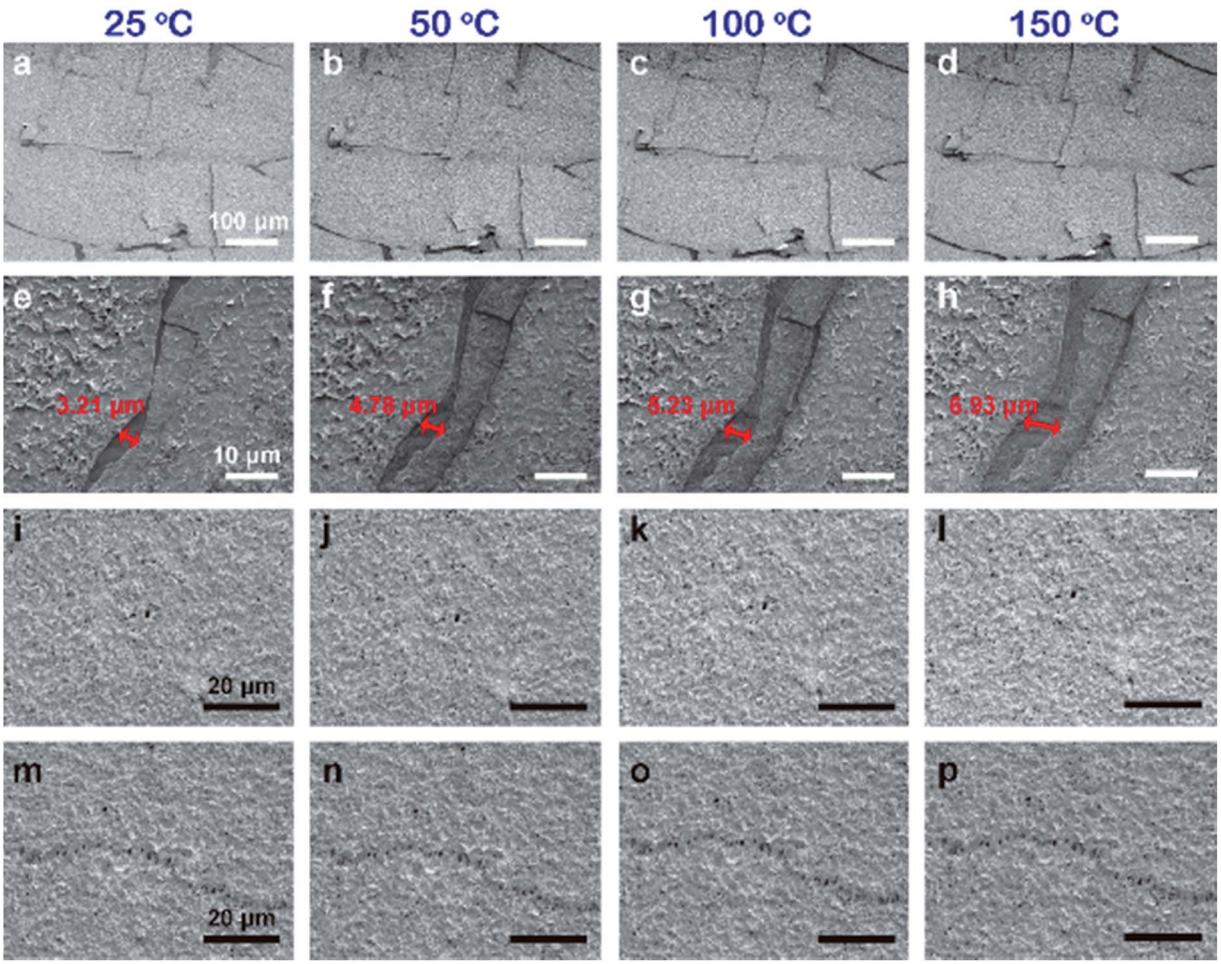

Fig. 4 Top view SEM images of the surface morphologies of the TMA-$Ti_3C_2T_x$ (a–h), HF6-d3-$Ti_3C_2T_x$ (i–l) and HF18-d2-$Ti_3C_2T_x$ (m–p) based sensors at different temperatures of 25, 50, 100, and 150 °C.

expansion of heating. The microstructure change of the local cracks on the film is characterized in Fig. 4e–h, S7 and Movie S1.† The cracks became much wider and longer at higher temperatures to release the tensile stress, which led to noteworthy destruction of conducting paths and rapid increases of the resistance. Therefore, TMA-$Ti_3C_2T_x$ based sensors demonstrated higher sensitivity. In contrast, the resistance of the HF6-d3-$Ti_3C_2T_x$ and HF18-d2-$Ti_3C_2T_x$ based sensors changed less because no cracks or fractures occurred during the heating process. Fig. 4i–l and m–p exhibit the top-view SEM images of the HF6-d3-$Ti_3C_2T_x$ and HF18-d2-$Ti_3C_2T_x$ based sensors under *in situ* heating, respectively. When PDMS expanded at higher temperatures, the nanoparticles slid to reduce the tensile stress so that the film extended without fractures. Although the sliding of nanoparticles induced resistance variations, the conductive path remained connective between the adjacent lamellae to keep the hybrid network stable and reduce the resistance changes. No obvious microstructure variations were observed at a high temperature of 150 °C, which explained the wide sensing ranges of the HF6-d3-$Ti_3C_2T_x$ and HF18-d2-$Ti_3C_2T_x$ based sensors.

These flexible sensors can be applied to multi-functional applications because of their high sensing performances. In addition to the monitoring of environmental temperatures, these sensors can also be used as e-skin for proximity detection. Because of their high sensitivity in response to radiation heat, the sensors can detect approaching objects without physically touching. The HF6-d3-$Ti_3C_2T_x$ based sensors with the pre-polymerization time of 10 min were chosen as the testing sample for the demonstration of the proximity detection. The results in Fig. 5a show that the resistance of the sensor increased when the finger was approaching the surface of the sensor. The relative resistance variation increased with the decrease of the distance between the finger and the sensor, which reached 1.91% at a distance of about 0.2 cm. The maximum distance that the sensor can detect is 9 cm with a relative resistance variation of 0.01%, indicating its wide application scope as highly sensitive e-skin. Repeatability is a desirable property for practical applications of e-skin as shown in Fig. 5b, suggesting that a noncontact sensor has great reproducibility with stable signal outputs. During this process, the radiant heat of the human skin made the temperature of the sample increase when the distance between the finger and

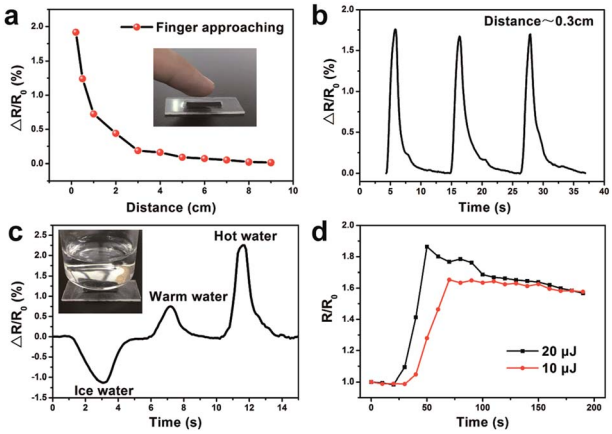

Fig. 5 (a) Resistance variation of the temperature sensor at different distances between the finger and the $Ti_3C_2T_x$ film; the inset shows the image of a finger approaching the sensor. (b) The repeatability of the proximity temperature sensor for 0.3 cm with three circles. (c) Resistance variation of the temperature sensor with the approach of vials containing ice, warm and hot water; the inset shows the image of a vial approaching the sensor. (d) Resistance variation of the temperature sensor using infrared lasers with different powers.

sample was about 0.3 cm. When removing the finger, the resistance decreased with the decrease of the temperature. To further demonstrate the possibility of monitoring the surface temperature of objects, we used vials containing ice, warm and hot water to approach the sensor. The output curve changed corresponding to the different temperatures of the vials (Fig. 5c). Except from the temperature of people and surroundings, the HF6-d3-$Ti_3C_2T_x$ based sensor can also detect the irradiation of infrared laser. Fig. 5d shows the resistance change of the temperature sensor using infrared lasers with different powers. The strain and resistance of the sensor increased at higher temperature. After reaching the saturation temperature, the strain and resistance reached their maximum value. Because of the elasticity of the PDMS substrate, the thermal expansion tended to decrease, which caused the decrease of the curves of the resistance variation after reaching the peaks. The relative resistance variation of the sensor using a laser of 20 μJ increased faster than that using a laser of 10 μJ. This specific performance suggests its possible utilization in a laser counter reconnaissance system.

How to eliminate the interference of other mechanical stimulus is a common challenge for most flexible sensors, including temperature and force sensors. For our temperature and proximity sensors, the non-contact sensing mode can ensure the reliability of the signals. Compared with the detection distance of 2 mm for the dual-parameter sensors,[60] our sensors presented a larger detection distance of 9 cm which could realize more practical applications. Furthermore, the pressure sensing performance of the sensors was investigated as shown in Fig. S8.† Compared with the high sensitivity for temperature sensing, the resistance increased slowly with respect to the pressure. The resistance change of the HF18-d2-$Ti_3C_2T_x$ sample was not obvious in a wide pressure range. Therefore, we can reduce the interference through device design and algorithm analysis in the contact sensing mode.

For full operational demonstration of e-skin, a 4×4 array of the temperature sensors was fabricated by transferring 16 pieces of $Ti_3C_2T_x$ films to the PDMS substrate. Ag electrodes were thermally evaporated through a shadow mask under vacuum for electric connections. As the conductivity of Ag is much higher than that of $Ti_3C_2T_x$, the influence of the resistance variations of electrodes on the sensing performance can be ignored during the tests. To model the temperature mapping on the sensor array, fingers, a vial containing warm water and an ultraviolet lamp were placed close to the top of the temperature sensor array as heat sources. The output resistance variation of each sensing pixel was recorded and plotted, displaying

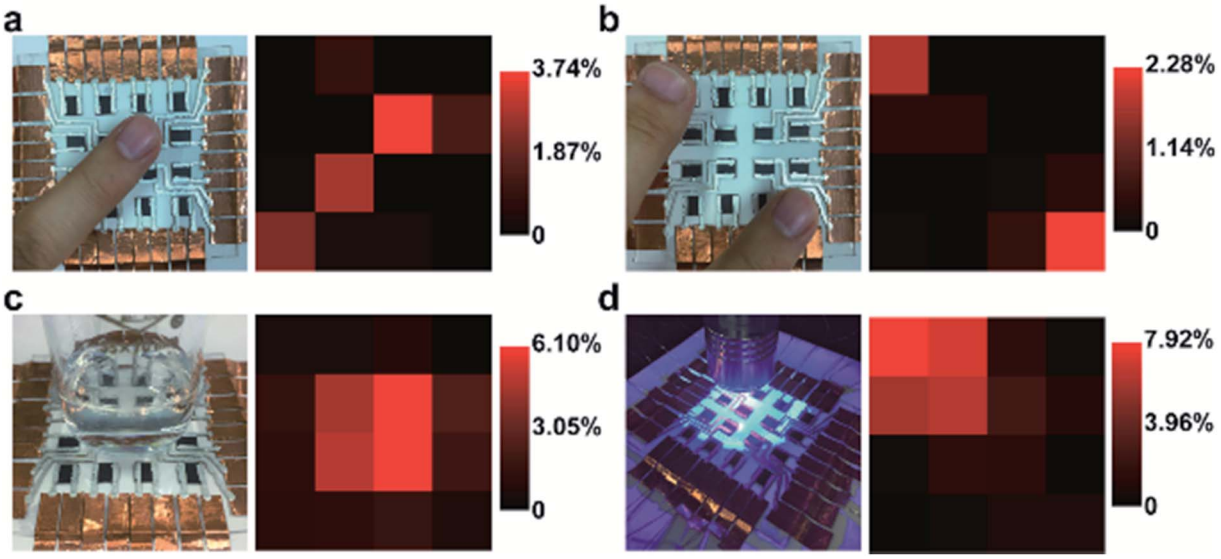

Fig. 6 The photographs and corresponding mapping of the temperature distribution *via* the measurement of the resistance variation by approaching the pixels with a finger (a), two fingers (b), a vial containing warm water (c), and an ultraviolet lamp (d).

spatial distributions of temperature through color contrast mapping as shown in Fig. 6a–d. The spatial distribution obtained was in accordance with the shapes of the heat sources, confirming the effective temperature mapping capability of our e-skin device. This precise temperature sensing performance of the sensor array demonstrates its potential to be applied in human–machine interfaces, prosthetics, and wearable skin electronics for monitoring of approaching objects and temperature variations during daily activities.

Conclusions

In summary, we proposed a facile fabrication strategy for highly flexible and sensitive temperature sensors based on $Ti_3C_2T_x$. As the sensing units, $Ti_3C_2T_x$ nanoparticles and $Ti_3C_2T_x$ lamellae were obtained simultaneously through controlling the process conditions. The temperature sensors based on $Ti_3C_2T_x$ with diverse morphologies and structures exhibited highly tunable sensing performances and a desirable combination of high sensitivity, wide working ranges, fast response time, high accuracies, and good cycling durability. In addition to the monitoring of environmental temperatures, the sensors can also be used as e-skin for proximity temperature detection. The utilization of the e-skin for temperature monitoring was demonstrated by a 4×4 sensing array, thus making our e-skin sensor a highly promising candidate for future applications such as human–machine interactions, smart prosthetics, and humanoid robots.

Experimental

Synthesis of the TMA-$Ti_3C_2T_x$ suspension

$Ti_3C_2T_x$ was prepared by chemical liquid etching. The Al layers in the precursor material Ti_3AlC_2 (200 meshes, from Forsman Co., China) were selectively etched with hydrofluoric acid (HF, 40 wt%, from China National Medicines Corporation Ltd.) or tetramethylammonium hydroxide (TMAOH, from Sigma). During the alkali etching process, Ti_3AlC_2 (1 g) powder was treated with 10 ml 20% HF under stirring (30 min) to remove the surface oxidant of Ti_3AlC_2. The resulting mixture was washed with distilled water and centrifuged until the pH was above 6. Then 12 ml 25% TAMOH was reacted with HF-treated Ti_3AlC_2 (1 g) for 24 h. The suspension was washed and collected by centrifugation to obtain TMA-intercalated $Ti_3C_2T_x$. The sediment was dispersed in 300 ml distilled water, delaminated by handshaking for 10 min, and centrifuged at 3500 rpm for 1 h to obtain the completely delaminated and large-scale $Ti_3C_2T_x$ (TMA-$Ti_3C_2T_x$).

Synthesis of the HF-$Ti_3C_2T_x$ suspension

During the acid etching process, the Ti_3AlC_2 powder was slowly immersed into 40% HF at a ratio of 1 g : 10 ml under continuous stirring for 6 h or 18 h at room temperature. The resulting mixture was washed with distilled water and centrifuged until the pH was above 6. The precipitates were then collected by vacuum filtration and dried using a vacuum freeze dryer, to obtain multilayer $Ti_3C_2T_x$ powder. Afterwards, 1 g of multilayer $Ti_3C_2T_x$ was added to 12 ml dimethylsulfoxide (DMSO, from China National Medicines Corporation Ltd.), and the mixture was stirred for 18 h. Subsequently, the DMSO was removed by centrifugal washing. Finally, the as-resulted sediment was added to 300 ml distilled water, which was followed by 3 or 2 h sonication and 1 h centrifugation at 3500 rpm. The supernatant containing delaminated $Ti_3C_2T_x$ (HF-$Ti_3C_2T_x$) was achieved in the final step.

Fabrication of the $Ti_3C_2T_x$ based temperature sensor

A certain amount of the as-prepared TMA-$Ti_3C_2T_x$ and the HF-$Ti_3C_2T_x$ suspension was vacuum filtered to form conductive films on mixed cellulose ester (MCE) membranes (diameter of 47 mm, pore size of 220 nm, from Merck Millipore Ltd.). Initially, the concentration of as-prepared TMA-$Ti_3C_2T_x$ and HF-$Ti_3C_2T_x$ was calibrated using the UV-visible spectrum to keep the same dosage of the $Ti_3C_2T_x$ suspension for each piece of the conductive film. The resulting film was dried under vacuum at 25 °C for 12 h. Polydimethylsiloxane (PDMS, a 10 : 1 mixture of the pre-polymer and curing agent, Sylgard-184, Dow Corning) was pre-polymerized by keeping at 80 °C for 5–15 min. Afterwards, the $Ti_3C_2T_x$/MCE membrane was attached onto the surface of PDMS with the $Ti_3C_2T_x$ side facing PDMS. The PDMS with the membrane was completely cured after a post-polymerization process (80 °C for 2 h). Subsequently, the $Ti_3C_2T_x$/PDMS composite film was prepared after dissolving the filter membrane in acetone. Finally, silver electrodes were coated on both ends of the $Ti_3C_2T_x$ film to complete the fabrication of the $Ti_3C_2T_x$ based temperature sensor.

Characterization and measurements

The phase composition and crystalline structure of samples were analyzed using a high-resolution multi-function X-ray diffractometer (D8 Discover Davinci, German). The concentration of the $Ti_3C_2T_x$ suspension was calibrated using an ultraviolet-visible spectrophotometer (PerkinElmer Lambda 950, USA). The size distribution of the $Ti_3C_2T_x$ suspension was obtained using an atomic force microscope (NTEGRA, NT-MDT, Russia). The morphologies at room temperature were characterized using a field emission scanning electron microscope (SU8220, Hitachi, Japan) and the *in situ* heating characterization was accomplished using an environmental scanning electron microscope (Quattro, Thermo Scientific). For testing the sensing performance, the temperature sensor was heated using a thermostatic hot plate and a digital thermometer was applied to measure the real-time temperature of the sample.

For testing the temperature-sensing properties, the sample was placed on a thermostatic heating stage and the probes of a digital thermocouple were brought into contact with the surface of a pure PDMS substrate to accurately detect the real-time temperature variation of the sample. The current signal was acquired using an electrochemical workstation (PARSTAT 2273, Princeton Applied Research). Then we increased the temperature of the stage with a heating rate of 1 °C s^{-1} and recorded the resistance and temperature change of the sample

to evaluate the sensing performance of the temperature sensor (Fig. S9†). The temperature measurements were also performed with an infrared imaging device (Fig. S10†). Because the infrared imaging is easily affected by the operating environment, the resistance variation is a little different from that measured using the thermocouple. To make the test results more precise, the temperature sensing performance is subject to the measurements of thermocouples.

Informed consent was obtained for the experiments involving human participants as shown in Fig. 5 and 6.

Conflicts of interest

There are no conflicts to declare.

Acknowledgements

We appreciate the support of National Natural Science Foundation of China (Grant No. 61871368), Youth Innovation Promotion Association CAS, Shanghai Science and Technology Rising Star Project (17QA1404700), and Young Elite Scientists Sponsorship Program by CAST.

Notes and references

1 S. K. Lee, B. J. Kim, H. Jang, S. C. Yoon, C. Lee, B. H. Hong, J. A. Rogers, J. H. Cho and J. H. Ahn, *Nano Lett.*, 2011, **11**, 4642–4646.
2 W. H. Yeo, Y. S. Kim, J. Lee, A. Ameen, L. K. Shi, M. Li, S. D. Wang, R. Ma, S. H. Jin, Z. Kang, Y. G. Huang and J. A. Rogers, *Adv. Mater.*, 2013, **25**, 2773–2778.
3 J. H. Lee, K. Y. Lee, M. K. Gupta, T. Y. Kim, D. Y. Lee, J. Oh, C. Ryu, W. J. Yoo, C. Y. Kang, S. J. Yoon, J. B. Yoo and S. W. Kim, *Adv. Mater.*, 2014, **26**, 765–769.
4 S. Xu, Y. H. Zhang, L. Jia, K. E. Mathewson, K. I. Jang, J. Kim, H. R. Fu, X. Huang, P. Chava, R. H. Wang, S. Bhole, L. Z. Wang, Y. J. Na, Y. Guan, M. Flavin, Z. S. Han, Y. G. Huang and J. A. Rogers, *Science*, 2014, **344**, 70–74.
5 T. Yokota, P. Zalar, M. Kaltenbrunner, H. Jinno, N. Matsuhisa, H. Kitanosako, Y. Tachibana, W. Yukita, M. Koizumi and T. Someya, *Sci. Adv.*, 2016, **2**, e1501856.
6 D. Chen and Q. Pei, *Chem. Rev.*, 2017, **117**, 11239–11268.
7 J. H. Koo, S. Jeong, H. J. Shim, D. Son, J. Kim, D. C. Kim, S. Choi, J. I. Hong and D. H. Kim, *ACS Nano*, 2017, **11**, 10032–10041.
8 R. S. Johansson and J. R. Flanagan, *Nat. Rev. Neurosci.*, 2009, **10**, 345–359.
9 W. M. Tiest, *Vis. Res.*, 2010, **50**, 2775–2782.
10 R. Ackerley, H. Olausson, J. Wessberg and F. McGlone, *Neurosci. Lett.*, 2012, **522**, 73–77.
11 V. E. Abraira and D. D. Ginty, *Neuron*, 2013, **79**, 618–639.
12 B. C. K. Tee, A. Chortos, A. Berndt, A. K. Nguyen, A. Tom, A. McGuire, Z. L. C. Lin, K. Tien, W. G. Bae, H. L. Wang, P. Mei, H. H. Chou, B. X. Cui, K. Deisseroth, T. N. Ng and Z. N. Bao, *Science*, 2015, **350**, 313–316.
13 R. C. Webb, Y. J. Ma, S. Krishnan, Y. H. Li, S. Yoon, X. G. Guo, X. Feng, Y. Shi, M. Seidel, N. H. Cho, J. Kurniawan, J. Ahad, N. Sheth, J. Kim, J. G. Taylor, T. Darlington, K. Chang, W. Z. Huang, J. Ayers, A. Gruebele, R. M. Pielak, M. J. Slepian, Y. G. Huang, A. M. Gorbach and J. A. Rogers, *Sci. Adv.*, 2015, **1**, e1500701.
14 D. S. Lee, J. Y. Shin, P. D. Tonge, M. C. Puri, S. Lee, H. Park, W. C. Lee, S. M. Hussein, T. Bleazard, J. Y. Yun, J. Kim, M. Li, N. Cloonan, D. Wood, J. L. Clancy, R. Mosbergen, J. H. Yi, K. S. Yang, H. Kim, H. Rhee, C. A. Wells, T. Preiss, S. M. Grimmond, I. M. Rogers, A. Nagy and J. S. Seo, *Nat. Commun.*, 2014, **5**, 5619–5628.
15 S. Bauer, S. Bauer-Gogonea, I. Graz, M. Kaltenbrunner, C. Keplinger and R. Schwodiauer, *Adv. Mater.*, 2014, **26**, 149–162.
16 S. Gong, W. Schwalb, Y. Wang, Y. Chen, Y. Tang, J. Si, B. Shirinzadeh and W. Cheng, *Nat. Commun.*, 2014, **5**, 3132–3139.
17 L. Sheng, Y. Liang, L. Jiang, Q. Wang, T. Wei, L. Qu and Z. Fan, *Adv. Funct. Mater.*, 2015, **25**, 6545–6551.
18 M. A. Darabi, A. Khosrozadeh, R. Mbeleck, Y. Q. Liu, Q. Chang, J. Z. Jiang, J. Cai, Q. Wang, G. X. Luo and M. Xing, *Adv. Mater.*, 2017, **29**, 1700533.
19 Y. Ma, N. Liu, L. Li, X. Hu, Z. Zou, J. Wang, S. Luo and Y. Gao, *Nat. Commun.*, 2017, **8**, 1207.
20 Y. Ma, Y. Yue, H. Zhang, F. Cheng, W. Zhao, J. Rao, S. Luo, J. Wang, X. Jiang, Z. Liu, N. Liu and Y. Gao, *ACS Nano*, 2018, **12**, 3209–3216.
21 Y. Yue, N. Liu, W. Liu, M. Li, Y. Ma, C. Luo, S. Wang, J. Rao, X. Hu, J. Su, Z. Zhang, Q. Huang and Y. Gao, *Nano Energy*, 2018, **50**, 79–87.
22 G. Ge, Y. Zhang, J. Shao, W. Wang, W. Si, W. Huang and X. Dong, *Adv. Funct. Mater.*, 2018, **28**, 1802576.
23 Y. Guo, M. Zhong, Z. Fang, P. Wan and G. Yu, *Nano Lett.*, 2019, **19**, 1143–1150.
24 C. L. Choong, M. B. Shim, B. S. Lee, S. Jeon, D. S. Ko, T. H. Kang, J. Bae, S. H. Lee, K. E. Byun, J. Im, Y. J. Jeong, C. E. Park, J. J. Park and U. I. Chung, *Adv. Mater.*, 2014, **26**, 3451–3458.
25 S. Jung, J. H. Kim, J. Kim, S. Choi, J. Lee, I. Park, T. Hyeon and D. H. Kim, *Adv. Mater.*, 2014, **26**, 4825–4830.
26 L. Pan, A. Chortos, G. Yu, Y. Wang, S. Isaacson, R. Allen, Y. Shi, R. Dauskardt and Z. Bao, *Nat. Commun.*, 2014, **5**, 3002–3009.
27 Y. Zang, F. Zhang, D. Huang, X. Gao, C.-a. Di and D. Zhu, *Nat. Commun.*, 2015, **6**, 6269–6277.
28 M. Jian, K. Xia, Q. Wang, Z. Yin, H. Wang, C. Wang, H. Xie, M. Zhang and Y. Zhang, *Adv. Funct. Mater.*, 2017, **27**, 1606066.
29 J. Jeon, H. B. Lee and Z. Bao, *Adv. Mater.*, 2013, **25**, 850–855.
30 S. Y. Hong, Y. H. Lee, H. Park, S. W. Jin, Y. R. Jeong, J. Yun, I. You, G. Zi and J. S. Ha, *Adv. Mater.*, 2016, **28**, 930–935.
31 T. Li, L. Li, H. Sun, Y. Xu, X. Wang, H. Luo, Z. Liu and T. Zhang, *Adv. Sci.*, 2017, **4**, 1600404.
32 T. Q. Trung, L. T. Duy, S. Ramasundaram and N.-E. Lee, *Nano Res.*, 2017, **10**, 2021–2033.
33 J. Zhang, X. Liu, G. Neri and N. Pinna, *Adv. Mater.*, 2016, **28**, 795–831.

34 J. Wu, K. Tao, Y. Guo, Z. Li, X. Wang, Z. Luo, S. Feng, C. Du, D. Chen, J. Miao and L. K. Norford, *Adv. Sci.*, 2017, **4**, 1600319.
35 C. Q. Yu, H. Wang and Y. X. Xia, *Appl. Phys. Lett.*, 2009, **95**, 263506.
36 S. F. Lin, T. J. Ding, J. T. Liu, C. C. Lee, T. H. Yang, W. Y. Chen and J. Y. Chang, *Sensors*, 2011, **11**, 8953–8965.
37 D. H. Kim, S. D. Wang, H. Keum, R. Ghaffari, Y. S. Kim, H. Tao, B. Panilaitis, M. Li, Z. Kang, F. Omenetto, Y. G. Huang and J. A. Rogers, *Small*, 2012, **8**, 3263–3268.
38 H. Cong, F. Yang, C. Xue, K. Yu, L. Zhou, N. Wang, B. Cheng and Q. Wang, *Small*, 2018, **14**, e1704414.
39 X. Ren, P. K. Chan, J. Lu, B. Huang and D. C. Leung, *Adv. Mater.*, 2013, **25**, 1291–1295.
40 J. S. Lee, K. Y. Shin, O. J. Cheong, J. H. Kim and J. Jang, *Sci. Rep.*, 2015, **5**, 7887.
41 S. Harada, K. Kanao, Y. Yamamoto, T. Arie, S. Akita and K. Takei, *ACS Nano*, 2014, **8**, 12851–12857.
42 S. Harada, W. Honda, T. Arie, S. Akita and K. Takei, *ACS Nano*, 2014, **8**, 3921–3927.
43 T. Q. Trung, S. Ramasundaram, S. W. Hong and N.-E. Lee, *Adv. Funct. Mater.*, 2014, **24**, 3438–3445.
44 C. Y. Yan, J. X. Wang and P. S. Lee, *ACS Nano*, 2015, **9**, 2130–2137.
45 Y. Chen, B. Lu, Y. Chen and X. Feng, *Sci. Rep.*, 2015, **5**, 11505.
46 M. D. Dankoco, G. Y. Tesfay, E. Benevent and M. Bendahan, *Mater. Sci. Eng., B*, 2016, **205**, 1–5.
47 W. Honda, S. Harada, T. Arie, S. Akita and K. Takei, *Adv. Funct. Mater.*, 2014, **24**, 3299–3304.
48 X. Wu, Y. Ma, G. Zhang, Y. Chu, J. Du, Y. Zhang, Z. Li, Y. Duan, Z. Fan and J. Huang, *Adv. Funct. Mater.*, 2015, **25**, 2138–2146.
49 X. Ren, K. Pei, B. Peng, Z. Zhang, Z. Wang, X. Wang and P. K. Chan, *Adv. Mater.*, 2016, **28**, 4832–4838.
50 T. Q. Trung, S. Ramasundaram, B. U. Hwang and N. E. Lee, *Adv. Mater.*, 2016, **28**, 502–509.
51 N. T. Tien, S. Jeon, D. I. Kim, T. Q. Trung, M. Jang, B. U. Hwang, K. E. Byun, J. Bae, E. Lee, J. B. H. Tok, Z. N. Bao, N. E. Lee and J. J. Park, *Adv. Mater.*, 2014, **26**, 796–804.
52 X. Zhao, Y. Long, T. Yang, J. Li and H. Zhu, *ACS Appl. Mater. Interfaces*, 2017, **9**, 30171–30176.
53 J. Park, M. Kim, Y. Lee, H. S. Lee and H. Ko, *Sci. Adv.*, 2015, **1**, e1500661.
54 W. P. Shih, L. C. Tsao, C. W. Lee, M. Y. Cheng, C. Chang, Y. J. Yang and K. C. Fan, *Sensors*, 2010, **10**, 3597–3610.
55 J. Yang, D. Wei, L. Tang, X. Song, W. Luo, J. Chu, T. Gao, H. Shi and C. Du, *RSC Adv.*, 2015, **5**, 25609–25615.
56 D. H. Ho, Q. Sun, S. Y. Kim, J. T. Han, D. H. Kim and J. H. Cho, *Adv. Mater.*, 2016, **28**, 2601–2608.
57 X. Liao, Q. Liao, Z. Zhang, X. Yan, Q. Liang, Q. Wang, M. Li and Y. Zhang, *Adv. Funct. Mater.*, 2016, **26**, 3074–3081.
58 M. Tian, Y. Huang, W. Wang, R. Li, P. Liu, C. Liu and Y. Zhang, *J. Mater. Res.*, 2014, **29**, 1288–1294.
59 J. Bang, W. S. Lee, B. Park, H. Joh, H. K. Woo, S. Jeon, J. Ahn, C. Jeong, T. i. Kim and S. J. Oh, *Adv. Funct. Mater.*, 2019, 1903047.
60 F. Zhang, Y. Zang, D. Huang, C. Di and D. Zhu, *Nat. Commun.*, 2015, **6**, 8356.